Hot Deformation Behavior and Processing Maps of As-Cast Hypoeutectic Al-Si-Mg Alloy

Zhenglong Liang, Qi Zhang, Liqun Niu, and Wei Luo

The hot deformation behavior of as-cast hypoeutectic Al-Si-Mg alloy has been investigated through hot compression tests at temperatures between 573 and 773 K and the strain rate of 0.001-1 s^{-1}. A modified Hansel-Spittel constitutive model is proposed, which takes the effect of strain rate on strain hardening into account. The processing maps are established based on the dynamic material model and the Murty criterion. Microstructure observations show that dynamic recovery dominates the dynamic softening behavior, and recrystallized grains are found in the sample tested at 773 K with strain rate of 0.01 and 0.001 s^{-1}. The size of Si particles decreases by about 64.73% with the effective strain increasing from 0 to 1.2. The optimal hot processing parameters of as-cast hypoeutectic Al-Si-Mg alloy are established based on the processing maps.

1. Introduction

Hypoeutectic aluminum alloys with silicon amount of 7-9% are the most widely used foundry alloys in automotive and aerospace applications due to their high strength-to-weight ratio, good castability and possibility of precipitation strengthening (Ref 1-4). The mechanical properties of those alloys greatly depend on the morphology and distribution of Si phase and primary aluminum dendrites as well as casting defects (Ref 5, 6). Severe plastic deformation methods, such as friction stir process (Ref 7), hot extrusion (Ref 8), equal channel angular pressing (Ref 9) and casting-forging process (Ref 10, 11), were found to be effective in refining casting features and eliminate casting defects, thereby enhancing mechanical properties (Ref 12). In order to acquire uniform and defect-free microstructure, it is quite necessary to investigate hot deformation behavior and evaluate workability of those alloys for optimizing the forming parameters of the processes.

Constitutive model is an effective method to depict the relationship between the deformation behavior and external loadings, such as strain, strain rate and temperature. In recent years, many constitutive models have been proposed to delineate the hot deformation behavior of those alloys (Ref 13). Haghdadi et al. proposed a strain-compensated Arrhenius-type constitutive model for modeling the flow behavior of A356 alloy at elevated temperature (Ref 14). A modified Johnson-Cook constitutive model for Al-Si-Mg alloy which takes the effect of strain rate on thermal softening into account was developed by Liang Ref 15. Lin et al. established a

physical-based constitutive model to predict the flow stress of a Sr-modified Al-Si-Mg alloy (Ref 16). Haghdadi et al. constructed an artificial neural network for modeling the mechanical properties of A356 alloy, and they found the ANN model can accurately predict the flow behavior (Ref 17). Those constitutive models can be put into three categories: phenomenological constitutive model, physical-based constitutive model and artificial neural network model (Ref 18). Compared with physical-based models, the phenomenological models involve less material constants, and the required experiments for phenomenological models could be conducted more easily (Ref 19). Therefore, the phenomenological models are widely used in both engineering practice and finite element software. Among various phenomenological models, the Hansel-Spittel model characterizes with concise equation format, is easier to calibrate than others and is employed to delineate the deformation behavior of the as-cast A356 alloy in this research.

Processing map can also be applied to evaluate the workability, optimize processing parameters and understand kinetics of metallurgical evolutions (Ref 20-22). Based on atomic mechanisms, Raj extended the concept of Ashby's maps to processing map construction, which is most effective for pure crystalline materials and simple alloys (Ref 23). However, it is difficult to simulate the response of complex engineering alloys through simple atomic mechanism models. Prasad et al. proposed another model, dynamic material model (DMM), to delineate the material deformation behavior during hot deformation (Ref 24). This model is widely used to construct processing maps of various materials for optimizing processing route and controlling their microstructures (Ref 25-29). Hu et al. Ref 30 constructed hot processing maps of Al-Si eutectic alloy at strain ranging from 0.1 to 0.5 and found that the instability region decreased while strain increased. Gangolu et al. Ref 31 found that the instability region in the processing map, by adding B_4C into Al-Si-Mg alloy, obviously enlarged with the increase in strain. Liao et al. Ref 32 reported the influence of Si content on processing maps of Al-Si-Mg alloy and found that the instability region of the alloy with 7 wt.% Si is the largest among those with Si of 0.6, 7 and 12.3 wt.%. In those studies, the efficiency of power dissipation (η) was expressed as $2m/(m + 1)$, where m is the strain rate sensitivity

Zhenglong Liang, Qi Zhang, Liqun Niu, and Wei Luo, School of Mechanical Engineering, Xi'an Jiaotong University, Xi'an 710049, China. Contact e-mail: henryzhang@mail.xjtu.edu.cn.

parameter. And the instability region was calculated through Prasada equation (Ref 33). The above equations are valid based on the power law assumption. However, there are still a large amount of constitutive equations which are not completely in line with the power law assumption. In such cases, the efficiency of power dissipation should be calculated by the following equation:

$$\eta = 2\left[1 - \frac{1}{\sigma\dot{\varepsilon}}\int_0^{\dot{\varepsilon}}\sigma\mathrm{d}\dot{\varepsilon}\right] \qquad \text{(Eq 1)}$$

where σ is the flow stress and $\dot{\varepsilon}$ is the strain rate. And the instability region can be calculated through Murty criterion $(2m < \eta)$ (Ref 34).

In the present study, isothermal compression tests of as-cast hypoeutectic Al-Si-Mg alloy were conducted to investigate its deformation behavior and processing maps during the hot deformation. A modified Hansel-Spittel constitutive model taken influence of strain rate on the strain hardening into account was developed, which was then applied in FEM program to simulate the hot compression process. Based on the dynamic material model and Murty criterion, processing maps at different strain states were established to study the hot workability of this material at its as-cast state.

2. Materials and Methods

The as-cast hypoeutectic Al-Si-Mg alloy was chosen as the experimental material, and its chemical composition is listed in Table 1. Cylindrical specimens were machined from a casting ingot of 10 mm diameter and 15 mm height. The isothermal compression tests were conducted using a Gleeble-3800 thermo-mechanical simulator at various temperatures (573, 623, 673 and 773 K) and strain rates (0.001, 0.01, 0.1 and 1 s^{-1}). Samples were firstly heated to the preset temperature at the heating rate of 5 °C s^{-1} and then soaked for 2 min to eliminate the temperature gradient inside. All samples were compressed to the required strain level, after which came immediate water quenching. In order to avoid oxidation of the specimen, the chamber was kept in vacuum state during the heating and compressing process. An extremely thin tantalum plate was utilized to minimize friction, as well as to prevent the adhesion of the specimen on the compression anvils.

The FORGE$^{\circledR}$ software was applied to simulate the hot compression process. The deformed samples were sectioned paralleling to the compression axis along the direction of centerline. Metallographic samples were polished and etched by Keller's solution. The metallurgical examinations were conducted by an optical microscope (Nikon LV150N). The size of Si particles at different deformation regions was measured. Specimens for EBSD were mechanically polished initially and then polished by the Multifunctional Ion Milling (Leica EM RES102) for 1 h. The orientation imaging microscopy maps were measured through electron backscattering diffraction

(EBSD) by a Hitachi SU3500 tungsten filament scanning electron microscope. In the orientation maps, high-angle boundaries (HABs) were defined to be larger than or be equal to 15° in misorientation while the low-angle boundaries (LABs) were defined to have a misorientation between 2° and 15°. HABs and LABs were depicted in orientation maps as white and purple lines, respectively.

3. Results

3.1 Flow Behavior

Measured true stress-strain curves of the hypoeutectic AL-Si-Mg alloy at various strain rates and temperatures are shown in Fig. 1. It can be observed that the flow stress, at the early deformation stage, sharply increased with strain rising, reaching to the peak in a short time. Then, the flow stress gradually decreased and went into a steady state. This phenomenon is caused by the competition between work hardening and dynamic softening during the hot compression. At the initial deformation stage, dislocations at impenetrable obstacles and forest dislocations propagated and accumulated dramatically, and work hardening dominated the deformation process. At the same time, the stored energy accumulated rapidly with the increase in strain, which provided the driving force for dynamic recovery in terms of dislocation climb and dislocation cross-slip, or even dynamic recrystallization. This is the primary mechanism for dynamic softening. Thus, dynamic recovery and recrystallization dominated the softening process during the declining period of flow stress curves. The latter steady state is the result of dynamic equilibrium between work hardening and dynamic softening.

3.2 Hansel-Spittel Model

The Hansel-Spittel constitutive model is employed to delineate the flow behavior in this research. The original Hansel-Spittel model can be expressed as Eq 2

$$\sigma = Ae^{m_1 T}\varepsilon^{m_2}\dot{\varepsilon}^{m_3}e^{(m_4/\varepsilon)}(1+\varepsilon)^{m_5 T}e^{m_7\varepsilon}\dot{\varepsilon}^{m_8 T}T^{m_9} \qquad \text{(Eq 2)}$$

where σ is the equivalent (Von Misses) flow stress, ε is the equivalent plastic strain, T is the deformation temperature, e is the natural constant and A, m_1, m_2, m_3, m_4 m_5, m_7 m_8 and m_9 are material coefficients, which can be determined by nonlinear regression analysis of measured true stress-strain data. Results are shown in Table 2.

Figure 2 shows the comparison between measured curves and those predicted by the original Hansel-Spittel model at different strain rates. It can be found that the gap between the predicted values and the measured data was greatly influenced by strain rate. As shown in Fig. 2(a), at strain rate of 1 s^{-1}, predicted values were larger than experimental ones at the initial state and smaller in rest parts. With the strain rate decreasing to 0.1 s^{-1}, the predicted flow stress accurately fits

Table 1   Chemical composition of the hypoeutectic Al-Mg-Si alloy (wt.%)

Si	Mg	Fe	Cu	Mn	Zn	Cr	Ti	Al
7.43	0.433	0.295	0.170	0.0687	0.0193	0.0107	0.0128	Balance
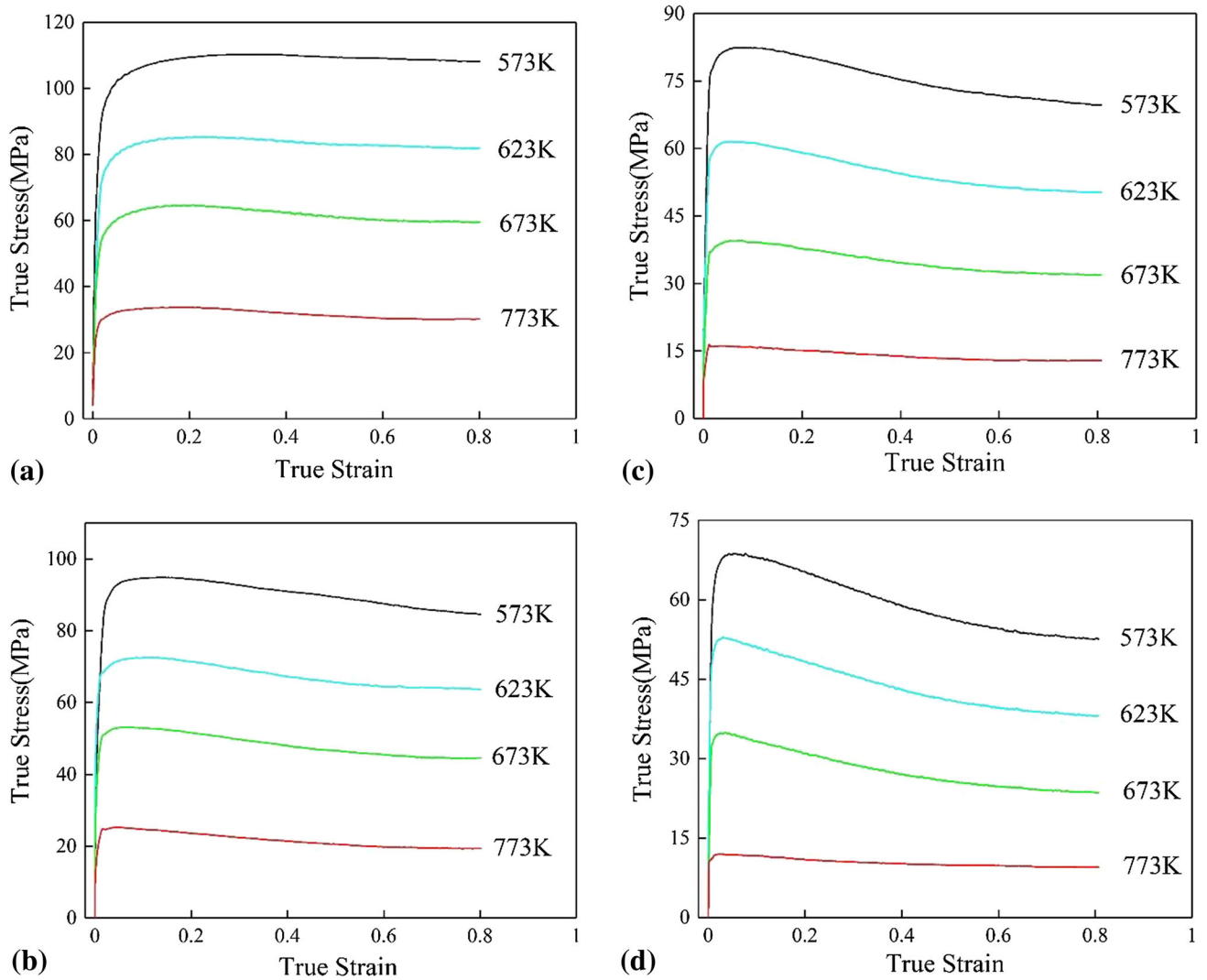
Fig. 1 The measured true stress-strain curves of the hypoeutectic Al-Si-Mg alloy at different strain rates (a) 1 s^{-1}, (b) 0.1 s^{-1}, (c) 0.01 s^{-1} and (d) 0.001 s^{-1}

Table 2 Material parameters of the Hansel-Spittel model for hypoeutectic Al-Si-Mg alloy

A	m_1	m_2	m_3	m_4	m_5	m_7	m_8	m_9
0.00334	-0.01246	0.02882	-0.03443	0	-0.00133	0.01842	0.00037	2.50268

the measured data. When the strain rate further falls to 0.01 and 0.001 s^{-1}, predicted values were smaller than experimental ones at the initial state and larger in rest parts. Obviously, predicted values were also influenced by plastic strain.

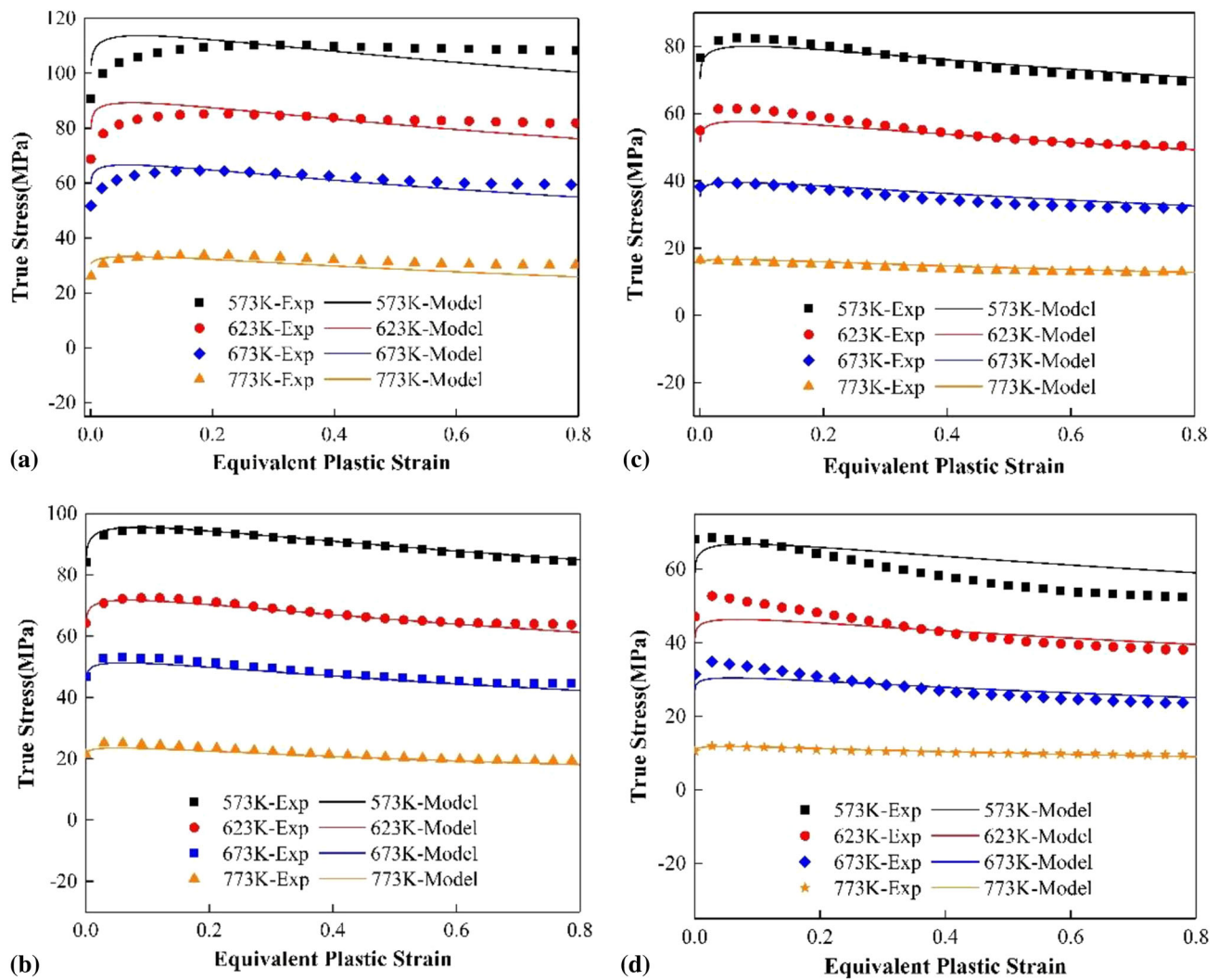### 3.3 Modified Hansel-Spittel Model

Aiming at achieving more accurate prediction, it is necessary to modify the original Hansel-Spittel model. It can be found that the influence of strain rate on strain hardening was not considered in original model. Therefore, to delineate the flow stress more accurately, its effect was incorporated into the original model by assuming that the plastic strain exponents in the original model are polynomial functions of strain rate. As

the strain hardening exponent has more remarkable impact on strain hardening, only m_2 and m_5 were selected.

$$m_2 = f_1(\dot{\varepsilon}) \tag{Eq 3}$$

$$m_5 = f_2(\dot{\varepsilon}) \tag{Eq 4}$$

The nonlinear regression analysis of measured true stress-strain data was conducted once again to determine the value of m_2 and m_5 at different strain rates. During the fitting process, only the material parameters m_2 and m_5 are variables, while other material parameters are kept as constants, which equal to those obtained in the original model. The value of m_2 and m_5 at various strain rates is shown in Table 3.

Fig. 2 Comparison between measured curves and the flow stress predicted by the original Hansel-Spittel model at different strain rates: (a) 1 s^{-1}, (b) 0.1 s^{-1}, (c) 0.01 s^{-1} and (d) 0.001 s^{-1}

Table 3 The values of m_2 and m_5 at various strain rate states

	$\dot{\varepsilon} = 1$	$\dot{\varepsilon} = 0.1$	$\dot{\varepsilon} = 0.01$	$\dot{\varepsilon} = 0.001$
m_2	0.0491	0.02882	0.0188	0.012
m_5	− 0.001	− 0.00133	− 0.00143	− 0.00173

Fitting the relationship between m_2, m_5 and $\ln(\dot{\varepsilon})$, it can be observed that both m_2 and m_5 can be exactly expressed by the cubic function of $\ln(\dot{\varepsilon})$. Fitting results are shown in Fig. 3. The R-Squares of those two fittings equal to 1, and the fitted parameters are illustrated in Table 4.

In order to verify the modified model, another group of hot compression tests were conducted at 723 K under the same conditions as previous tests. Comparison between new measured curves and the flow stress curves predicted by the modified Hansel-Spittel model is shown in Fig. 4. It is obvious that the modified model can predict the flow behavior of the hypoeutectic Al-Si-Mg alloy more accurately than the original model.

3.4 Processing Maps

According to the dynamic material model (Ref 24), the material underwent hot deformation can be considered as a dissipater of power, and the total energy (P) can be divided into two parts: G content (temperature rise) and J co-content (microstructure mechanisms), which can represent the function of flow stress, strain and strain rate:

$$P = \sigma\dot{\varepsilon} = G + J = \int_0^{\dot{\varepsilon}} \sigma d\dot{\varepsilon} + \int_0^{\sigma} \dot{\varepsilon} d\sigma \qquad (\text{Eq } 5)$$

The power partitioning between J and G is determined by the strain rate sensitivity (m), which is usually expressed by a differential function of stress and strain rate at specific plastic strain. The equation is as following:

$$m = dJ/dG = \dot{\varepsilon}d\sigma/\sigma d\dot{\varepsilon} = d(\ln \sigma)/d(\ln \dot{\varepsilon}) \qquad (\text{Eq } 6)$$

For an ideal linear dissipater, $m = 1$ and $J_{max} = \sigma\dot{\varepsilon}/2$. Besides, the parameter η is defined to describe the efficiency of power dissipation by the following equation:

$$\eta = J/J_{max} = (P - G)/J_{max} = 2\left(1 - \int_0^{\dot{\varepsilon}} \sigma d\dot{\varepsilon}/\sigma\dot{\varepsilon}\right) \quad \text{(Eq 7)}$$

m and η can be calculated by applying the modified Hansel-Spittel model into Eq 6 and 7, and power dissipation efficiency maps can be developed by plotting the η values acquired under various deformation conditions on the temperature versus $\log(\dot{\varepsilon})$ system. The instability maps can be established according to Murty criterion ($2m < \eta$). The processing map of the hypoeutectic Al-Si-Mg alloy can be constructed through superimposing instability maps over the power dissipation efficiency maps at specified plastic strain.
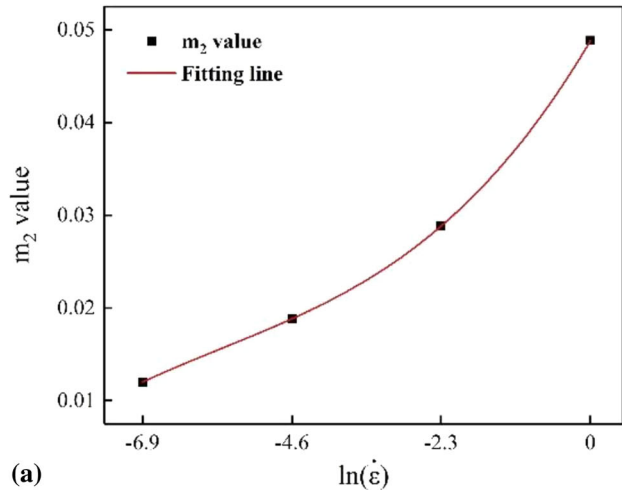
(a)
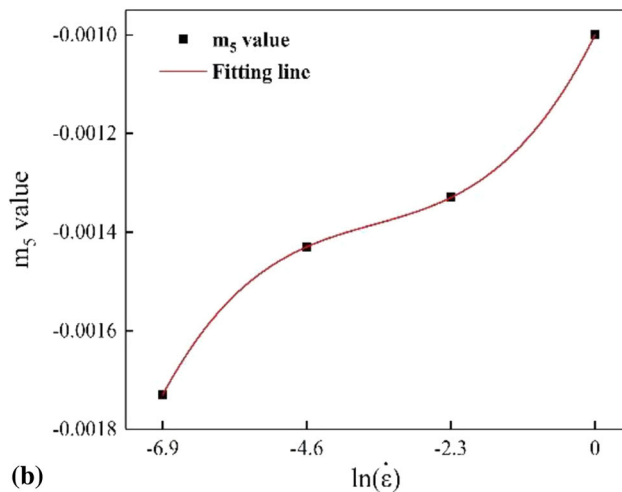
(b)

Fig. 3 Relationships between m_2, m_5 and $\ln(\dot{\varepsilon})$: (a) m_2 vs. $\ln(\dot{\varepsilon})$ and (b) m_5 vs. $\ln(\dot{\varepsilon})$

Table 4 The fitted parameters of the relationship between m_2, m_5 and $\ln(\dot{\varepsilon})$

$m = A + B \ln(\dot{\varepsilon})$ $+ C \ln(\dot{\varepsilon})^2 + D \ln(\dot{\varepsilon})^3$	A	B	C	D
m_2	0.0491	0.01184	0.00159	0.000093
m_5	− 0.001	0.000256	0.000062	0.0000059

The processing maps of the as-cast hypoeutectic Al-Si-Mg alloy at various plastic strains with the strain rates of 0.001-1 s^{-1} and temperatures of 573-773 K are illustrated in Fig. 5. In those maps, the counter line label represents the power dissipation efficiency (η), while the shadow regions represent the instability regions ($2m < \eta$). It can be found from Fig. 5(a) that there was no instability region in the processing map at a plastic strain of 0.2. As illustrated in Fig. 5(b), there was a very small instability region when the plastic strain is 0.4. The instability region gradually enlarged with the plastic strain increasing from 0.4 to 0.8. Hot compression parameters of the instability regions were detected at temperatures of 573-650 K with strain rates of 0.001-0.0125 s^{-1}. Thus, it can be concluded that the hypoeutectic Al-Si-Mg alloy in the present work should not be hot deformed under above-mentioned conditions. Similar results are observed in other studies on Al-Si-Mg alloy (Ref 30, 32).

As illustrated in Fig. 5, the peak efficiency of power dissipation increased with the plastic strain rising. When the plastic strain increased from 0.2 to 0.8, the peak efficiency of power dissipation increased from 0.28 to 0.38, i.e., a rising of about 35.7%. The power dissipation efficiency also increased with the rising of the deformation temperature. With the hot compression temperature increasing from 573 to 773 k, the power dissipation efficiency increased about 100% at all four strain levels. At the same time, it is clear that the power dissipation efficiency decreased with increasing of strain rate at low strain rate state ($\dot{\varepsilon} \leq 0.1$ s^{-1}), while it increased with strain rate at the higher strain rate state ($\dot{\varepsilon} \geq 0.1$ s^{-1}). It is well known that higher power dissipation efficiency always corresponds to better hot workability of materials. Therefore, the interaction among plastic strain, strain rate and deformation temperature and their effects on hot workability of alloys should be taken into consideration when designing the processing routes.

3.5 Microstructure Evolution

The deformed sample can be divided into three regions based on deformation conditions: (I) hard deformation region, (II) free deformation region and (III) severe deformation region (Ref 35). The FORGE® was used to analyze the effective strain
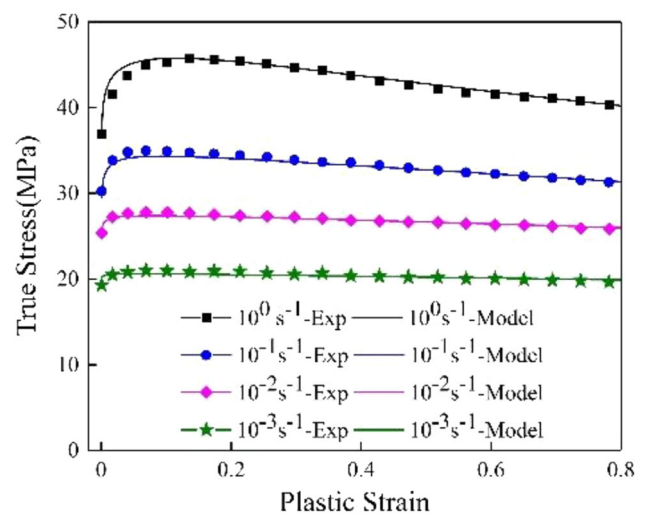
Fig. 4 Comparison between the measured curves and the flow stress curves predicted by the modified Hansel-Spittel model at 723 K
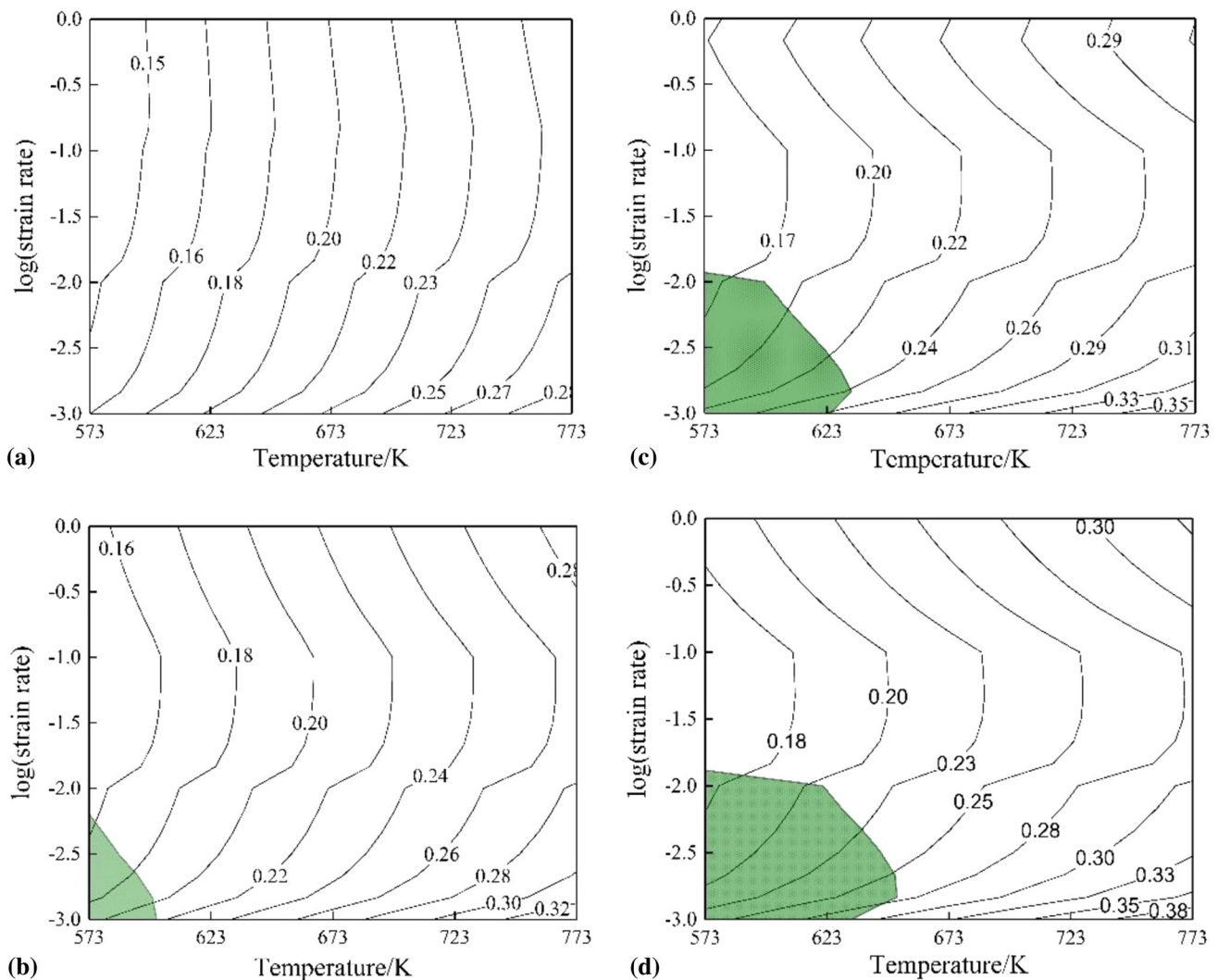
Fig. 5 Processing maps of as-cast hypoeutectic Al-Si-Mg alloy developed at plastic strain of (a) 0.2, (b) 0.4, (c) 0.6 and (d) 0.8

distribution during the hot compression process. Figure 6(a) shows the effective strain distribution of the sample deformed at 773 K with a strain rate of 1 s^{-1}. Obviously, the sample can also be divided into three regions according to the effective strain distribution. As shown in Fig. 6(a), the effective strain of region I was the smallest, which can be considered as the hard deformation region. The effective strain of region II was around 0.6-0.75, and the region II should correspond to the free deformation region. The effective strain of region III was the largest; hence, it belongs to the severe deformation region. Mechanical properties of the hypoeutectic Al-Si-Mg alloy greatly depend on the morphology and distribution of Si phase and primary dendrites. In order to evaluate the evolution of the casting features during the hot deformation process, both primary casting features and deformed microstructures at different regions were measured by optical microscopy, which are shown in Fig. 6(b), (c), (d) and (e).

As shown in Fig. 6(b), the microstructure of the original material was dominated by primary casting dendrites, which were surrounded by Si phase, exhibiting a typical casting microstructure. Same features can be found in region I, as

shown in Fig. 6(c). From Fig. 6(d) and (e), it can be observed that the casting features were destroyed in both free deformation region and severe deformation region. In these two regions, both primary plate-like and long-strip Si particles were fragmented and are more randomly distributed in the Al matrix.

The orientation imaging microscopy maps in the severe deformation region under different deformation conditions are shown in Fig. 7. The black strips in figures are Si particles. Figure 7(a) shows that lower angle boundaries dominated the microstructure at 573 K. With deformation temperature increasing to 723 K, a few equiaxed grains with large angle boundary were found, as shown in Fig. 7(b), exhibiting a typical characteristic of dynamical recrystallization. As illustrated in Fig. 7(c), with temperature further increasing to 773 K, the amount of recrystallization grains increased significantly. Figure 7(d) shows the microstructure deformed at 773 K with a strain rate of 0.01 s^{-1}. With the strain rate increasing from 0.001 to 0.01 s^{-1}, there was no enough time for the newly formed grains to grow. Therefore, the microstructure deformed at 773 K with a strain rate of 0.01 s^{-1} characterized by smaller grains than that at 773 K with strain rate of 0.001 s^{-1}.
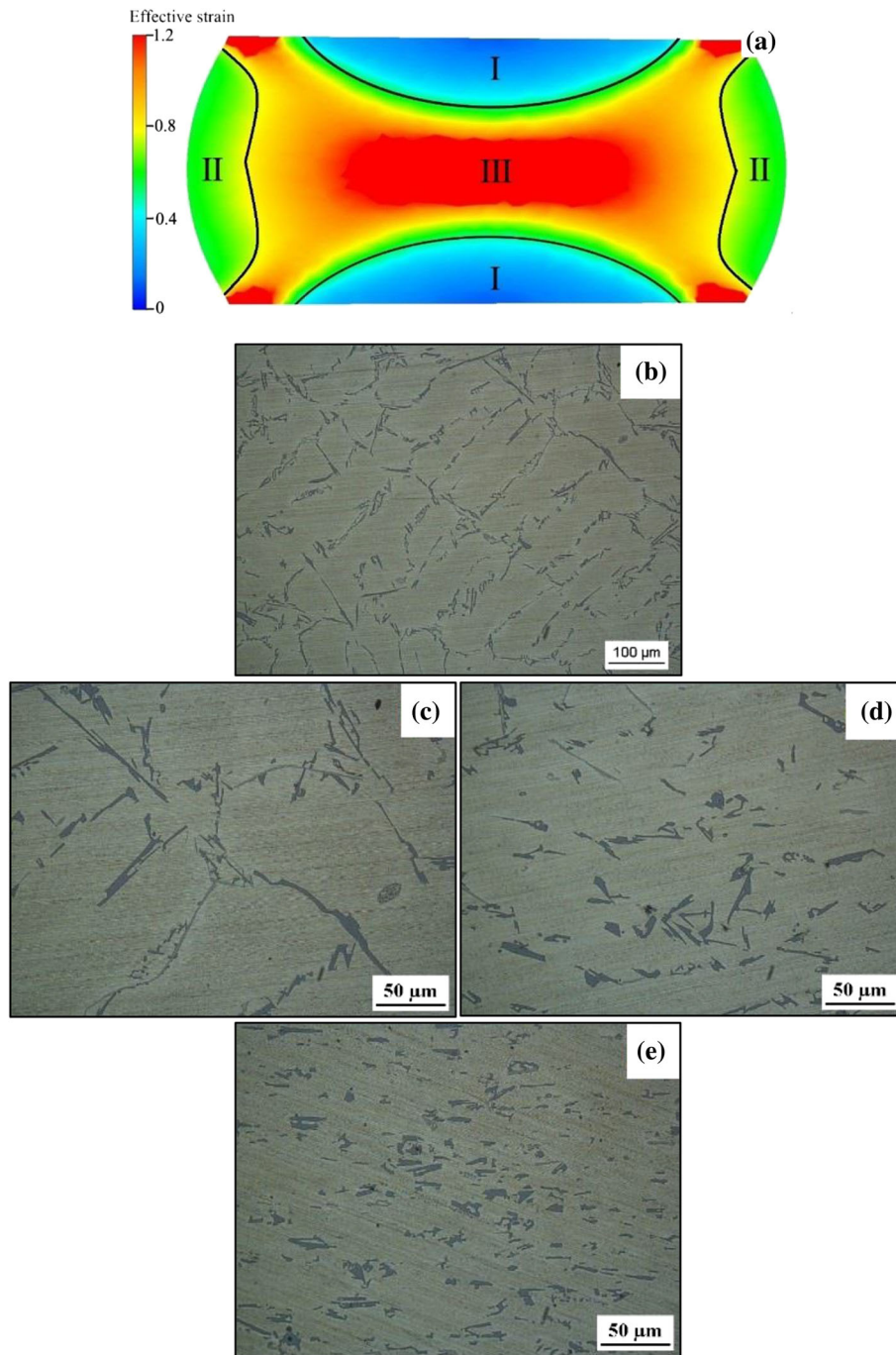
Fig. 6 The effective strain distribution of the hypoeutectic Al-Si-Mg sample (a), the microstructure of the original material (b), the microstructure of region I (c), region II (d) and region III (e)

4. Discussion

4.1 Material Deformation Behavior

Flow behavior of as-cast hypoeutectic Al-Si-Mg alloy at various strain rates and temperatures has been studied in the present research. It can be observed form Fig. 1 that the flow stress decreases with the increase in deformation temperature and the falling of strain rate. In order to evaluate the influence of deformation temperature and strain rate on dynamic softening behavior, dynamic softening ratio was introduced. The dynamic softening ratio can be calculated through

$$S = \frac{\sigma_p - \sigma_s}{\sigma_p} \times 100\% \qquad (Eq\ 8)$$

where S is the dynamic softening ratio, σ_p is the peak value of flow stress and σ_s is the flow stress at steady state.

The effects of deformation temperature and strain rate on dynamic softening ratio are shown in Fig. 8. It can be found from Fig. 8 that the dynamic softening ratio increased with deformation temperature rising, and it decreased with the strain rate rising. It is widely recognized that dynamic recovery and dynamic recrystallization dominate the dynamic softening of
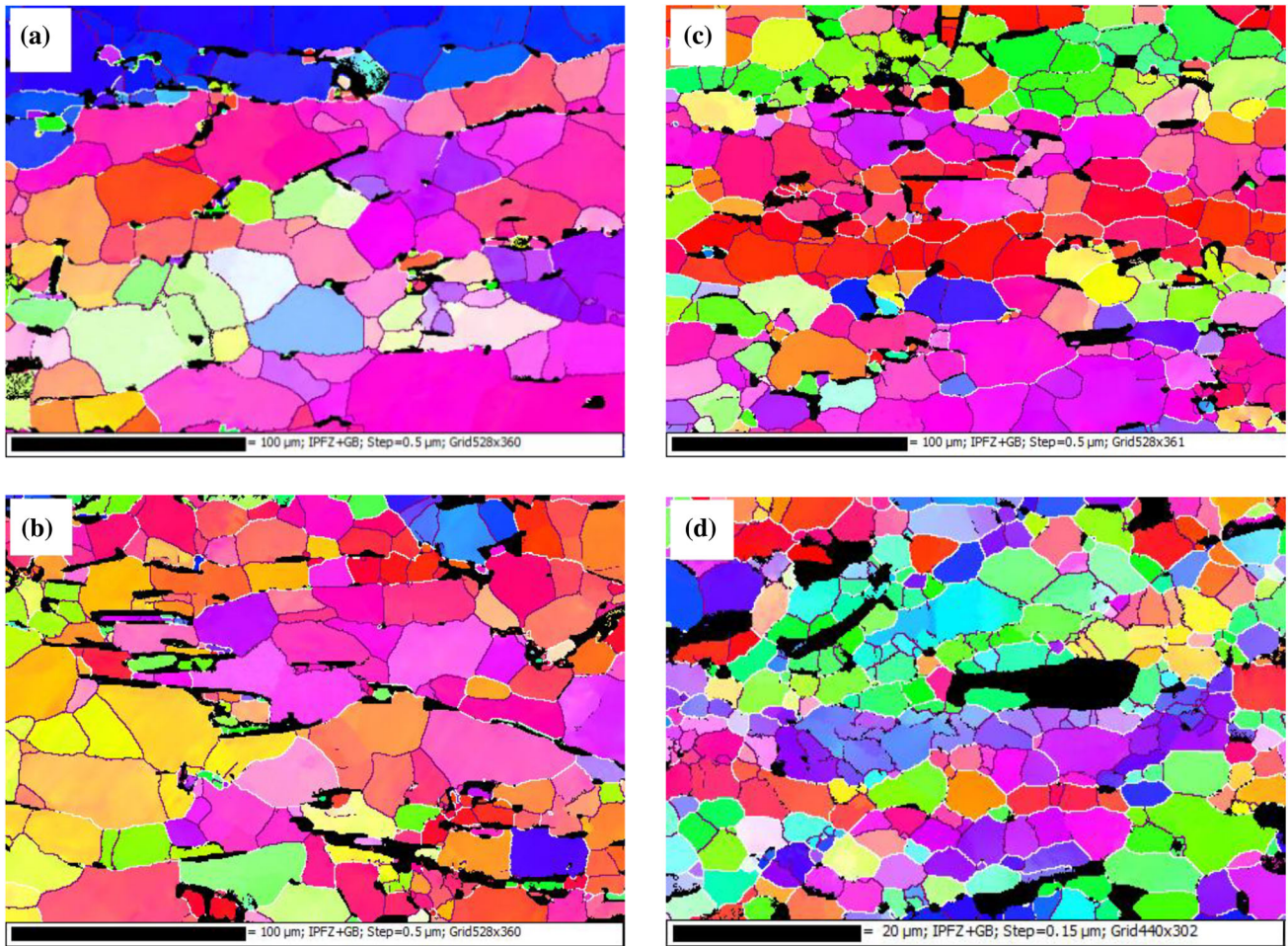
Fig. 7 EBSD microstructure of hypoeutectic Al-Si-Mg alloy under different deformation conditions: (a) 573 K + 0.001 s^{-1}, (b) 723 K + 0.001 s^{-1}, (c) 773 K + 0.001 s^{-1} and (d) 773 K + 0.01 s^{-1}

aluminum alloy during hot deformation process. At lower deformation temperature and higher strain rate, dynamic recovery and recrystallization by cross-slip and climbing of dislocation are retarded, for which the dislocation density was kept high, resulting in a higher flow stress and lower dynamic softening ratio. With the decreasing of the strain rate and increasing of deformation temperature, time for energy accumulation and dislocation annihilation was prolonged, and dynamic recovery and dynamic recrystallization were facilitated. This can be confirmed by the EBSD maps in Fig. 7. At the same time, the microstructure softening, dynamic coarsening and dissolution of strengthening phase such as Mg$_2$Si particles at high temperature can also exert positive effects on the softening behavior.

The material coefficients of the original Hansel-Spittel model were determined through nonlinear regression of experimental data. However, the original Hansel-Spittel model cannot accurately predict the flow stress curve. Considering the fact that the fitting precision of the original model greatly depends on strain rate and plastic strain, a modified Hansel-Spittel model, in which the effect of strain rate on strain hardening is taken into account, was established. This modified model was proved to predict more accurate than the original model.

4.2 Si Phase Evolution

In order to evaluate the effect of hot plastic deformation on morphology of Si particles, the average size of Si particles in all categorized regions was measured, and the results are shown in Fig. 9. The size of Si particles remarkably decreased with the increase in effective strain. In the region with effective strain below 0.3 (region I), the average size decreased by only 6.98%, while the figure was 39.14% in region II, in which the effective strain was between 0.6 and 0.75. When the effective strain increases further to the severe deformation region, a dramatic decrease in particle size ($\sim$ 64.73%) would occur.

The fragmentation of Si particles can be explained by both thermal and mechanical effects. During hot deformation, the thermal expansion coefficient difference between Si particles and Al matrix can generate thermal stress at the interface between Si particles and Al matrix (Ref 36), which can lead to brittle fracture of Si particles. At the same time, thermal degradation, occurring at local crystal defects such as holes and fissures in plate-like Si particles, is also responsible for such fragmentation (Ref 37). On the other hand, the strain incompatibility is developed near the interface between Si particles and Al matrix due to their different elastic constants and deformation behavior (Ref 38), which may cause cracking of Si particles. Furthermore, the plastic deformation also contributes
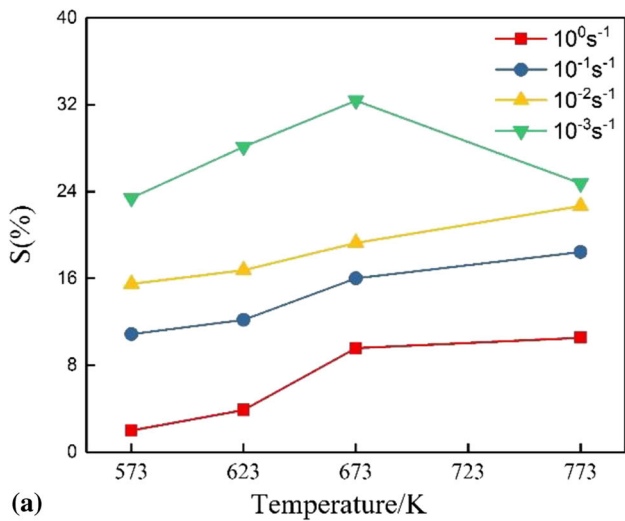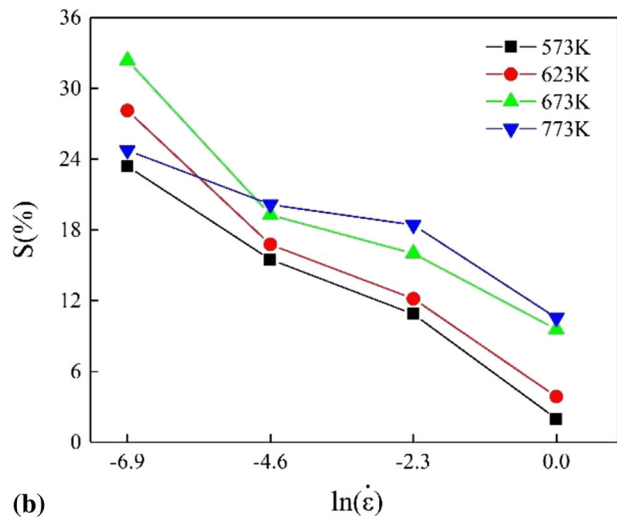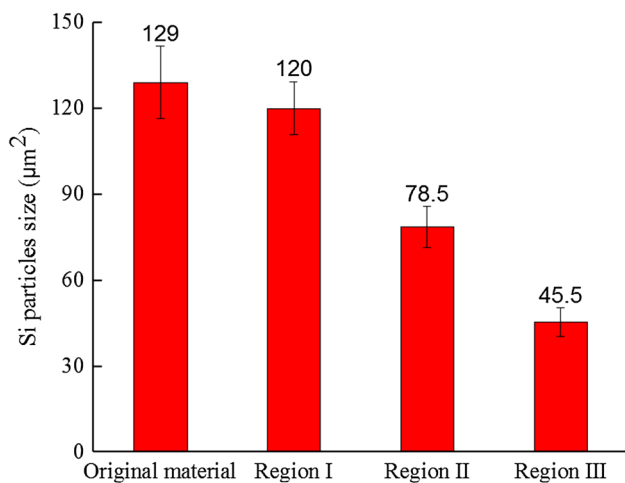
Fig. 8 Effects of deformation conditions on dynamic softening ratio: (a) temperature and (b) strain rate

Fig. 9 Size of Si particles in different regions

to the refinement of Si particles significantly due to their poor ductility.

4.3 Hot Workability

According to the modified Hansel-Spittel model, the flow stress at specific strain and temperature cannot be expressed by power law. Thus, the efficiency of power dissipation should be calculated by Eq 1 rather than by the equation $\eta = 2m/(m + 1)$, and the instability region is determined based on Murty criterion in the present research. The optimal workability and microstructure of materials can always be obtained under the highest power dissipation efficiency at safe regions of the processing maps. As illustrated in Fig. 5(b), (c) and (d), the highest efficiency of power dissipation occurred in low strain rate ($0.001 \, \text{s}^{-1} < \dot{\varepsilon} \leq 0.01 \, \text{s}^{-1}$) and high deformation temperature ($660 \, K < T \leq 773 \, K$) regions. In high strain rate ($0.1 \, \text{s}^{-1} < \dot{\varepsilon} \leq 1 \, \text{s}^{-1}$) and high deformation temperature ($740 \, K < T \leq 773 \, K$) regions, the power dissipation efficiency was larger than 0.3 at plastic strain of 0.6 and 0.8. Therefore, those two regions should be considered as optimum conditions for hot working of the hypoeutectic Al-Si-Mg alloy.

The instability region occurs at lower strain rate (0.001-0.01 s^{-1}) with temperature ranging from 573 to 650 K. Generally, the instability mechanism is probably associated with local plastic flow, adiabatic shear bands and voiding. However, as shown in Fig. 6 and 7, the existence of those areas is not supported on the basis of microstructure observation. But the crack is evident in the sample tested at temperature 573 K with a strain rate of 0.001 s^{-1}, and the angle between the compression axis and direction of crack propagation is 45°, as illustrated in Fig. 10. Therefore, it can be concluded that cracking is the main contributor for instability of the hypoeutectic Al-Si-Mg alloy.

5. Conclusions

The hot deformation behavior of as-cast hypoeutectic Al-Si-Mg alloy has been investigated through hot compression tests at temperature ranging 573-773 K and strain rate ranging 0.001-1 s^{-1}. A modified Hansel-Spittel constitutive model is proposed based on experimental measured data, which were used to establish the processing maps for strains of 0.2, 0.4, 0.6 and 0.8. The following conclusions can be drawn:

(1) The dynamic recovery and recrystallization is the main dynamic softening mechanism for as-cast hypoeutectic Al-Si-Mg alloy during hot deformation. The dynamic recrystallization occurs at temperature of 723-773 K with strain rate of 0.001-0.01 s^{-1}.

(2) A modified Hansel-Spittel model which takes the effect of strain rate on strain hardening into account is established, and the comparison between the predicted data and measured one shows that the modified model can predict the flow behavior more accurately.

(3) FEM method is used to analyze the morphology evolution of Si particles during the hot plastic deformation, the results show that the size of Si particles decreases by 39.14% at the region where effective strain ranges from 0.6 to 0.75 while it decreases by 64.73% at the region with effective strain of 1.2.

Fig. 10 Tested sample at (a) 573 K + 0.001 s^{-1} and (b) 573 K + 1 s^{-1}

(4) Instability region increases with plastic strain and occurs at temperature of 573-623 K with strain rate of 0.001-0.01 s^{-1}. The optimal hot working parameters of as-cast hypoeutectic Al-Si-Mg alloy are deformation temperature of 660-773 K with strain rate of 0.001-0.01 s^{-1}, and deformation temperature of 740-773 K with strain rate of 0.001-0.01 s^{-1}.

References

1. P. Pandee, C.M. Gourlay, S.A. Belyakov, U. Patakham, G. Zeng, and C. Limmaneevichitr, AlSi$_2$Sc$_2$ Intermetallic Formation in Al-7Si-0.3Mg-xSc Alloys and Their Effects on As-Cast Properties, *J. Alloy. Compd.*, 2018, **731**, p 1159–1170

2. B. Lin, H.Y. Li, R. Xu et al., Effects of Vanadium on Modification of Iron-Rich Intermetallics and Mechanical Properties in A356 Cast Alloys with 1.5 wt.% Fe, *J. Mater. Eng. Perform.*, 2019, **28**(1), p 475–484

3. Y. Zhang, H.L. Zheng, Y. Liu, L. Shi, R.F. Xu, and X.L. Tian, Cluster-Assisted Nucleation of Silicon Phase on Hypoeutectic Al-Si Alloy with Further Inoculation, *Acta Mater.*, 2014, **70**, p 162–173

4. W.D. Zhang, Y. Liu, J. Yang, J.Z. Dang, H. Xu, and Z.M. Du, Effects of Sc Content on the Microstructure of As-Cast Al-7 wt.% Si Alloys, *Mater. Charact.*, 2012, **66**, p 104–110

5. Z.N. Chen, H.J. Kang, G.H. Fan et al., Grain Refinement of Hypoeutectic Al-Si Alloys with B, *Acta Mater.*, 2016, **120**, p 168–178

6. C. Xu, F. Wang, H. Mudassar et al., Effect of Sc and Sr on the Eutectic Si Morphology and Tensile Properties of Al-Si-Mg Alloy, *J. Mater. Eng. Perform.*, 2017, **26**(4), p 1605–1613

7. P.R. Guru, F. Khan, S.K. Panigrahi et al., Enhancing Strength, Ductility and Machinability of a Al-Si Cast Alloy by Friction Stir Processing, *J. Manuf. Process.*, 2015, **18**, p 67–74

8. M.M. Marin, A.M. Camacho, and J.A. Pérez, Influence of the Temperature on AA6061 Aluminum Alloy in a Hot Extrusion Process, *Proc. Manuf.*, 2017, **13**, p 327–334

9. K.N. Campo, C.T.W. Proni, and E.J. Zoqui, Influence of the Processing Route on the Microstructure of Aluminum alloy A356 for Thixoforming, *Mater. Charact.*, 2013, **85**, p 26–37

10. S.C. Wang, N. Zhou, W.J. Qi, and K.H. Zheng, Microstructure and Mechanical Properties of A356 Aluminum Alloy Wheels Prepared by Thixo-Forging Combined with a Low Superheat Casting Process, *Trans. Nonferrous Met. Soc.*, 2014, **24**(7), p 2214–2219

11. H.T. Zhou, S.X. Xu, W.D. Li et al., A Study of Automobile Bracket Formed by Casting-Forging Integrated Forming Technology, *Mater. Des.*, 2015, **67**, p 285–292

12. Y. Liu, C. Geng, Q.Q. Lin et al., Study on Hot Deformation Behavior and Intrinsic Workability of 6063 Aluminum Alloys Using 3D Processing Map, *J. Alloy. Compd.*, 2017, **713**, p 121–221

13. Y.C. Lin, S.C. Luo, L.X. Yin et al., Microstructural Evolution and High Temperature Flow Behaviors of a Homogenized Sr-Modified Al-Si-Mg Alloy, *J. Alloy. Compd.*, 2018, **739**, p 590–599

14. N. Haghdadi, A. Zarei-Hanzaki, and H.R. Abedi, The Flow Behavior Modeling of Cast A356 Aluminum Alloy at Elevated Temperature Considering the Effect of Strain, *Mater. Sci. Eng. A-Struct.*, 2012, **535**, p 252–257

15. Z.L. Liang and Q. Zhang, Quasi-Static Loading Responses and Constitutive Modeling of Al-Si-Mg Alloy, *Metals*, 2018, **838**, p 1–11

16. Y.C. Lin, S.C. Luo, X.Y. Jiang et al., Hot Deformation Behavior of a Sr-Modified Al-Si-Mg Alloy: Constitutive Model and Processing Maps, *Trans. Nonferrous Met. Soc. China*, 2018, **28**, p 592–603

17. N. Haghdadi, A. Zarei-Hanzaki, A.R. Khalesian et al., Artificial Neural Network Modeling to Predict the Hot Deformation Behavior of an A356 Aluminum Alloy, *Mater. Des.*, 2013, **49**, p 386–391

18. Y.C. Lin and X.M. Chen, A Critical Review of Experimental Results and Constitutive Descriptions for Metals and Alloys in Hot Working, *Mater. Des.*, 2011, **32**, p 1733–1759

19. J.Q. Tian, M. Zhan, S. Liu et al., A Modified Johnson-Cook Model for Tensile Flow Behaviors of 7050-T7451 Aluminum Alloy at High Strain Rates, *Mater. Sci. Eng. A-Struct.*, 2015, **631**, p 214–219

20. R.Y. Lin, Y.U. Duan, L.S. Ma et al., Flow Behavior, Dynamic Recrystallization and Processing Map of Mg-20Pb-1.6Al-0.48B Alloy, *J. Mater. Eng. Perform.*, 2017, **26**, p 2439–2451

21. N. Ravichandran and Y.V.R.K. Prasad, Dynamic Recrystallization During Hot Deformation of Aluminum: A Study using Processing Maps, *Metall. Trans. A*, 1991, **22**(10), p 2339–2348

22. P.S. Robi and U.S. Dixit, Application of Neural Networks in Generating Processing Map for Hot Working, *J. Mater. Process. Technol.*, 2003, **142**(1), p 289–294

23. R. Raj, Development of a Processing Map for Use in Warm-Forming and Hot-Forming Processes, *Metall. Trans. A*, 1981, **12A**, p 1089–1097

24. Y.V.R.K. Prasad, H.L. Gegel, S.M. Doraivelu et al., Modeling of Dynamic Material Behavior in Hot Deformation-Forging of Ti-6242, *Metall. Trans. A*, 1984, **15**, p 1883–1892

25. Y. Liu, W. Xiong, Q. Yang et al., Constitutive Behavior and Processing Maps of T2 Pure Copper Deformed from 293 to 1073 K, *J. Mater. Eng. Perform.*, 2018, **27**(4), p 1812–1824

26. G.X. Wang, L. Xu, Y. Wang et al., Processing Maps for Hot Working Behavior of a PM TiAl Alloy, *J. Mater. Sci. Technol.*, 2011, **27**(10), p 893–898

27. K.T. Son, M.H. Kim, S.W. Kim et al., Evaluation of Hot Deformation Characteristics in Modified AA5052 Using Processing and Activation Energy Map Under Deformation Heating, *J. Alloy. Compd.*, 2018, **740**, p 96–108

28. Y.H. Duan, L.S. Ma, H.R. Qi et al., Developed Constitutive Models, Processing Maps and Microstructural Evolution of Pb-Mg-10Al-0.5B Alloy, *Mater. Charact.*, 2017, **129**, p 353–366

29. D.Y. Cai, L.Y. Xiong, W.C. Liu et al., Characterization of Hot Deformation Behavior of a Ni-Base Superalloy Using Processing Map, *Mater. Des.*, 2009, **30**(3), p 921–925

30. H.E. Hu, X.Y. Wang, and L. Deng, High Temperature Deformation Behavior and Optimal Hot Processing Parameters of Al-Si Eutectic Alloy, *Mater. Sci. Eng. A-Struct.*, 2013, **576**, p 45–51

31. S. Gangolu, A.G. Rao, I. Sabirov, B.P. Kashyap, N. Prabhu, and V.P. Deshmukh, Development of Constitutive Relationship and Processing Map for Al-6.65Si-0.44Mg Alloy and Its Composite with B$_4$C Particulates, *Mater. Sci. Eng. A-Struct.*, 2016, **655**, p 256–264

32. H.C. Liao, Y. Wu, K.X. Zhou, and J. Yang, Hot Deformation Behavior and Processing Map of Al-Mg-Si Alloys Containing Different Amount of Silicon Based on Gleebe-3500 Hot Compression Simulation, *Mater. Des.*, 2015, **65**, p 1091–1099

33. N. Ravichandran and Y.V.R.K. Prasad, Dynamic Recrystallization During Hot Deformation of Aluminum: A Study Using Processing Maps, *Metall. Trans. A*, 1991, **22**(10), p 2339–2348

34. S.V.S. Narayana Murty and B. Nageswara Rao, On the Flow Localization Concepts in The processing Maps of Titanium Alloy Ti-24Al-20Nb, *J. Mater. Process. Technol.*, 2000, **104**, p 103–109

35. X.W. Yang and W.Y. Li, Flow Behavior and Processing Maps of a Low-Carbon Steel During Hot Deformation, *Metall. Mater. Trans. A*, 2015, **46A**, p 6052–6064

36. S.K. Chaudhury and D. Apelian, Effects of Rapid Heating on Aging Characteristics of T6 Tempered Al-Si-Mg Alloys Using a Fluidized Bed, *J. Mater. Sci.*, 2006, **41**(14), p 4684–4690

37. L.J. Colley. Microstructure-Property Models for Heat Treatment of A356 Aluminum Alloy (Ph.D. Thesisi). University of British Columbia, Vancouver, Canada, 2011

38. S.W. Youn and C.G. Kang, Characterization of Age-Hardening Behavior of Eutectic Region in Squeeze-Cast A356-T6 Alloy Using Nanoindenter and Atomic Force Microscope, *Mater. Sci. Eng. A-Struct.*, 2006, **425**, p 28–35

Publisher's Note Springer Nature remains neutral with regard to jurisdictional claims in published maps and institutional affiliations.